Research Square

Preprints are preliminary reports that have not undergone peer review.
They should not be considered conclusive, used to inform clinical practice,
or referenced by the media as validated information.

Generation of two-wavelength superscattering and super-forward scattering from degenerate electric modes in four-layered dielectric/epsilon-near-zero nanoshells

Yan Li

Yanli@zua.edu.cn

[redacted]

Pengcheng Li

[redacted]

Yunzhe Li

[redacted]

ShuaiFu Zhao

[redacted]

Zhenchang Song

[redacted]

Xiyu Zhang

[redacted]

Chunxia Zhang

[redacted]

Li Shao

[redacted]

Facheng Zhong

[redacted]

Research Article

Keywords: superscattering, superdirectional scattering, Mie theory, four-layered nanoshells, degenerate epsilon-near-zero modes

Posted Date: November 24th, 2026

DOI: https://doi.org/10.21203/rs.3.rs-11722574/v1

License: This work is licensed under a Creative Commons Attribution 4.0 International License.
Read Full License

Additional Declarations: No competing interests reported.

Generation of two-wavelength superscattering and super-forward scattering from degenerate electric modes in four-layered dielectric/epsilon-near-zero nanoshells

Yan Li*, Pengcheng Li, Yunzhe Li, Shuaifu Zhao, Zhenchang Song, Xiyu Zhang, Chunxia Zhang, Li Shao, Facheng Zhong*

School of Materials, Zhengzhou University of Aeronautics, Zhengzhou 450046, China

*Corresponding author: Yanli@zua.edu.cn (Y. Li) and zfc@zua.edu.cn (F. Zhong)

Acknowledgements The authors gratefully acknowledge the financial support from Henan Provincial Science and Technology Research Project (Nos. 252102211125), the Key Scientific Research Project of Colleges and Universities in Henan Province (Grant No. 23ZX018), National College Students Innovation and Entrepreneurship Training Program (Grant Nos. 202610485066 and 202610485082), the Scientific Research Team Plan of Zhengzhou University of Aeronautics (Grant No. 24ZHTD01002).

Abstract

Superscattering, induced by degenerate modes in a subwavelength particle, has attracted considerable interest due to its unique optical properties with potential applications in optical tagging, nanoantennas, and spectroscopy. However, most studies on superscattering have focused on intensity enhancement, the directional control of superscattering, especially superdirectional scattering at two or more frequencies, remains largely unexplored and constitutes a substantial challenge. We propose a concentric core-shell nanoparticle, consisting of four alternating dielectric and aluminium-doped zinc oxide (AZO) layers with two different epsilon-near-zero (ENZ) points, that can realize superscattering with super-forward scattering near two ENZ wavelengths. We demonstrate that two Al:ZnO shells can support two electric ENZ modes (ENZMs) with the same angular momentum but different mode orders near their ENZ wavelengths. Depending on the mode order of the excited ENZMs, we show that such nanoparticles can strongly confine the electric fields within different Al:ZnO shell layers. By flexibly varying the structural parameters, both dielectric dipolar and quadrupolar resonances can be tuned to overlap at two ENZ wavelengths (degenerate ENZMs), enabling two-wavelength superscattering in such subwavelength nanoparticle. Furthermore, we demonstrate that through the interference of degenerate electric dipolar and quadrupolar ENZMs, two-wavelength super-forward

scattering can be achieved. This approach, relying on degenerate electric ENZMs in single subwavelength nanoparticle, offers a new pathway for constructing superscattering and superdirectional scattering, holding significant potential for applications in photovoltaic devices, biosensors, and nanoantennas.

Keywords: superscattering; superdirectional scattering; Mie theory; four-layered nanoshells; degenerate epsilon-near-zero modes

1. Introduction

The manipulation of light scattering, in both intensity and directionality, underpins a wide range of applications, including antenna design [1-3], energy harvesting [4,5], sensing [6,7], and imaging [8,11]. For most subwavelength scatterers, however, the scattering cross section is fundamentally bounded by the dipole single-channel scattering limit ($3\lambda^2/2\pi$ for a small 3D nanoparticle [12-14]). Since the total cross-section nevertheless grows with the number of channels that can be driven simultaneously, a scatterer whose resonances of different orders are brought into spectral coincidence can exceed that bound. This possibility was first established theoretically in 2010 via the degenerate resonance of multiple plasmonic eigenmodes using a plasmonic-dielectric multilayered cylindrical structure; the effect is referred to as superscattering [12]. It has since attracted sustained attention due to its potential for arbitrarily enhancing light scattering and its promising applications. In recent years, various multilayered structures [14-16], Hyperbolic Structures [17], and high-index dielectric core coated by indium antimonide [18] have been proposed to realize superscattering. Superscattering essentially provides a parallel means to leverage the scattering by spectrally overlapping scattering channels of different orders, which can also enhance the scattering in a given direction, however, the study on controlling the directionality of superscattering is still in its infancy [19].

Unidirectional sacttering is conventionally obtained through the interference of the electric and magnetic dipoles in a magnetoelectric particle, that is, the first ($a_1 = b_1$) or second ($a_1 = -b_1$) Kerker condition [20-24], and its generalizations extend this interference to higher-order electric and magnetic multipoles [25-27]. It has been shown that the scattering in backward or forward direction can be suppressed in a simple high permittivity nanosphere [22,24,25] or metallo-dielectric core-shell nanoparticles [21,26,27]. However, the electric dipole and magnetic dipole in most reported methods cannot surpass the single-channel scattering limit and the total scattering is still limited. More recently, Kerker superscattering based on the interference between a super electric dipole and a super magnetic dipole in a metasurface-coated dielectric resonator [28], and superscattering with near-zero forward scattering assisted by optical gain [29], have demonstrated superscattering and unidirectional scattering simultaneously, but they rely on

magnetic or gain-assisted responses. Such schemes require high-permittivity or gain materials and are difficult to extend to superdirectional scattering at two or more wavelengths. Since multi-wavelength unidirectional scattering would improve both accuracy and sensitivity in optical tagging, sensing, and spectroscopy [30,31], a route to superdirectional scattering at two or more wavelengths that relies on pure electric modes is highly desirable.

Epsilon-near-zero (ENZ) materials, whose permittivity has a near-zero real part, offer new opportunities for superdirectional scattering from subwavelength nanoparticles because of their exotic electromagnetic properties[32-36]. Especially, the effective wavelength inside an ENZ medium becomes extremely large, which produces "static-like" field distributions, allows ENZ-based antennas to exhibit size-invariant resonant responses, and leaves considerable freedom in antenna geometry [33-36]. Furthermore, electric and magnetic mode degeneracy, together with resonance nesting, has also been identified in dielectric cavities embedded in ENZ backgrounds, where modes of different orders share a common eigenfrequency [37]. The interference of these degenerate ENZ modes (ENZMs) offers a promising route to achieving super-directional scattering. More recently, a spherical ENZ nanoshell was shown to support degenerate electric dipole and quadrupole ENZMs and to exhibit super-forward scattering, using aluminum-doped zinc oxide (AZO) as ENZ material, with the effect tunable through the aluminum doping level of AZO and the shell geometry[38]. This raises an interesting question of whether a multilayered dielectric/ENZ core–shell particle can support both superscattering and super-forward scattering at two or more wavelengths at once — a question that, to our knowledge, remains open.

In this paper, we reveal that two-wavelength superscattering with near-zero backward scattering can be achieved simultaneously in a concentric core-shell nanoparticle, consisting of four alternating dielectric and AZO layers with different aluminum doping levels (corresponding to two different ENZ points). Such two AZO shells can support two electric ENZMs with the same angular momentum (mode number l) but different mode orders (m) near their different ENZ wavelengths. Depending on the mode order (m) of the excited ENZMs, the electric fields are confined within the different AZO shells that supply the corresponding ENZ point. Taking advantage of the fact that the resonances occur mainly near the ENZ wavelengths of the AZO layers and are independent of the mode number l, the electric dipolar and quadrupolar resonances can be tuned to overlap near two ENZ wavelengths (degenerate electric dipolar and quadrupolar ENZMs) by simply varying the structural parameters, enabling two-wavelength superscattering in such subwavelength nanoparticle. Furthermore, we demonstrate that through the interference of degenerate electric dipole and quadrupole ENZMs, two-wavelength super-forward scattering can be achieved. This approach, relying on

degenerate electric ENZMs in a single subwavelength nanoparticle, offers a new pathway for constructing superscattering with super-forward scattering, holding significant potential for applications in photovoltaic devices, biosensors, and nanoantennas.

2. Theory and methods

2.1. Geometry and material dispersion

Figure 1(a) shows the proposed four-layer concentric nanosphere, consisting of four alternating dielectric and semiconductor-based plasmonic layers (the core being considered as the first layer), that supports two-wavelength superscattering. The core radius (thickness of the first layer) is r_1, the outer radii of the three concentric shells are r_2, r_3 and r_4, and the corresponding layer permittivities are ε_1, ε_2, ε_3 and ε_4. Here, the second and fourth layers are chosen to be AZO with different aluminum doping levels, and their permittivity is taken to follow a Drude model

$$\varepsilon_{2,4}(\omega) = 3.3 - \frac{{\omega_{p2,4}}^2}{\omega^2 + \mathrm{i}\gamma\omega} \quad (1)$$

where $\omega_{p2,4}$ is the plasma frequency and γ is the collision frequency. The plasma frequency can be tuned by the aluminum doping level and can therefore be engineered independently in the two AZO layers. Following Refs. [30,38-40], we take $\omega_{p2} = 2213.2$ THz for the second layer and $\omega_{p4} = 1.1\omega_p$ for the fourth layer to yield two ENZ wavelengths (frequencies) in the near-infrared regime. Due to the relatively low losses in such semiconductor-based plasmonic materials, the collision frequency is taken as $\gamma = 4.43$ THz for both AZO layers [30,40,41]. Because the two plasma frequencies differ, the two AZO layers reach their ENZ points at different wavelengths, corresponding to a difference in permittivity $\Delta\varepsilon$ at a given wavelength (frequency). Figure 1(b) shows the real parts of the permittivities of the two AZO layers as a function of the incident wavelength. For the second layer ($\omega_{p2} = 2213.2$ THz), the ENZ point falls at $\lambda = 1545$ nm, whereas for the fourth layer ($\omega_{p4} = 1.1\omega_{p2}$) it falls at $\lambda = 1406$ nm. At $\lambda = 1545$ nm, the difference in permittivity for the second and fourth layers is $\Delta\varepsilon \approx 0.6$. The scattering problem of such a multilayer dielectric/AZO nanosphere embedded in an isotropic medium of permittivity ε_b (air, $\varepsilon_b = 1$, throughout this work) is solved analytically with Mie theory.

2.2. Mie theory and degenerate electric ENZMs of the multilayer sphere

The scattering efficiency Q_{sca} of the multilayer sphere can be decomposed into separate multipolar contributions[42]:

$$Q_{sca} = \frac{2}{k^2 r_4^2}\sum_{l=1}^{\infty}(2l+1)(|a_l|^2 + |b_l|^2) \quad (2)$$

where $k = 2\pi/\lambda$ is the wavenumber in the surrounding medium, r_4 is the outer radius of the nanosphere. a_l and b_l are the electric (transverse-magnetic, TM) and magnetic (transverse-electric, TE) Mie coefficients, where l corresponds to the angular momentum number (mode number). The contribution of a single electric channel is $Q_{sca}(a_l) = (2/k^2r_4^2)(2l+1)|a_l|^2$, and the single-channel limit for 3D scatter is $3\lambda^2/2\pi^2r_4^2$ [12-14] , which is the reference to determine whether superscattering has been achieved. In addition, the forward (Q_f) and backward (Q_b) scattering efficiency, corresponding to the scattering efficiency in the forward and backward directions, are defined as:

$$Q_f = \frac{1}{k^2 r_4^2}\left|\sum_l (2l+1)(a_l + b_l)\right|^2 \tag{3}$$

$$Q_b = \frac{1}{k^2 r_4^2}\left|\sum_l (-1)^l (2l+1)(a_l - b_l)\right|^2 \tag{4}$$

To understand the resonant behaviour of the alternating dielectric/plasmonic multilayer sphere and to design two-wavelength superscattering, the electric Mie coefficient a_l can be written as [30,38,40,43]

$$a_l = -\frac{U_l^{TM}}{U_l^{TM} + iV_l^{TM}} \tag{5}$$

where the U_l^{TM} and V_l^{TM} are obtained by solving $2N\times2N$ determinants, which are derived by applying the electromagnetic boundary conditions at the $N = 4$ spherical interfaces for the four-layer particle considered here [43]. When $V_l^{TM} = 0$, $a_l = -1$ and the maximum scattering for lth-order electric mode is achieved. The dispersion relation $V_l^{TM} = 0$ therefore provides the basis for our analysis of the resonant scattering of the lth-order electric mode. The degeneracy and interaction of different modes lead to the superscattering and superdirectional scattering features described in the paper.

We first consider equal shell thickness and neglect material loss, in which case the geometry of the structure is determined by the ratio $\eta_c = r_1/r_4$ of the core radius to the outer radius. In the thin-shell limit $\eta_c \to 1$, the quasi-static dispersion equation of the lth-order electric resonance, $V_l^{TM} = 0$, can be written in the simple form:

$$(\varepsilon_1 + 2\varepsilon_b)\,\varepsilon_3\,\varepsilon_2\,(\varepsilon_2 - \Delta\varepsilon) = 0 \tag{6}$$

The dispersion equation has two solutions, $\varepsilon_2 = 0$ and $\varepsilon_2 = \Delta\varepsilon$ ($\varepsilon_4 = \varepsilon_2 - \Delta\varepsilon = 0$), which depend solely on the ENZ points of the first and fourth plasmonic layers and are independent of the mode number l, indicating that the electric modes with different mode number l coincide at two different ENZ points of the two plasmonic shells and thus giving rise to two-wavelength degenerate ENZ modes (ENZMs). In the present four-layer geometry the ENZ condition is supplied by the two AZO layers, whose ENZ wavelengths are 1545 nm (second layer) and 1406 nm (fourth layer), so that these

two roots are reached at two distinct wavelengths. Consequently, in the thin-shell regime every electric multipole of the particle — the dipole, the quadrupole and, in principle, all higher orders — resonates at each of the two ENZ wavelengths simultaneously. Because several channels are then driven on resonance at the same wavelength, the total scattering of the particle is no longer capped by a single channel, and superscattering at two wavelengths becomes possible. Moreover, the interplay of these degenerate electric ENZMs can also induce superdirectional scattering. For instance, for a small nanoparticle where the scattering efficiency Q_{sca} is dominated by the contributions of the electric dipole (a_1) and quadrupole (a_2), when the two electric multipoles oscillate in phase and Mie term ($-3a_1+5a_2$) reaches zero, the backward scattering $Q_b = \frac{1}{k^2R^2}|-3a_1 + 5a_2|^2$ can be strongly suppressed (Eq. (4)), while the forward scattering efficiency $Q_f = \frac{1}{k^2R^2}|3a_1 + 5a_2|^2$ can be greatly increased (Eq. (3)).

3. Results and discussion

3.1. Degenerate ENZMs of the four-layer dielectric/AZO nanosphere

To validate the concept, we consider a multilayer nanosphere with an outer radius of r_4 = 320 nm ($r_4 \sim \lambda/5$), for which the quasi-static limit holds approximately. Although smaller particles satisfy the quasi-static approximation better, they are not considered here because, as the particle size decreases, higher-order modes are increasingly attenuated by material loss (see Fig. S1 in Supplementary Section 1), which prevents the total scattering from exceeding the single-channel limit. Using Eq. (2), we calculate the scattering efficiencies contributed by the electric dipole, $Q_{\mathrm{sca}}(a_1)$, and by the electric quadrupole, $Q_{\mathrm{sca}}(a_2)$, as functions of wavelength and of the core-to-outer radius ratio η_c, as shown in Figs. 1(c) and 1(d), respectively. The top axes in Figs. 1(c) and 1(d) give the real part of the wavelength-dependent permittivity of the second shell, ε_2. Both the electric dipole resonance [Fig. 1(c)] and the electric quadrupole resonance [Fig. 1(d)] occur near $\mathrm{Re}(\varepsilon_2) \approx 0$ and near $\mathrm{Re}(\varepsilon_2) \approx 0.6$ (corresponding to $\mathrm{Re}(\varepsilon_4) \approx 0$) when the shell is ultrathin ($\eta_c \to 1$), which means that two-wavelength degenerate ENZMs are generated, as predicted by Eq. (6). These four scattering modes are marked as $\mathrm{ENZM}_{1,1}$, $\mathrm{ENZM}_{1,2}$, $\mathrm{ENZM}_{2,1}$, and $\mathrm{ENZM}_{2,2}$, where the notation $\mathrm{ENZM}_{l,m}$ identifies each mode by its mode number l and mode order m. To visualize the spectral overlap of these modes, black contours marking the region where the electric quadrupole contribution to the scattering efficiency exceeds 0.1, $Q_{\mathrm{sca}}(a_2) > 0.1$, are superimposed on the dipole scattering-efficiency map in Fig. 1(e). As the shell thickness increases to about 30 nm (η_c = 0.72, the third horizontal black dashed line), both the dipole and the quadrupole ENZMs redshift simultaneously while remaining spectrally close, that is, nearly degenerate.

Figure 1(f) further presents the dipole and quadrupole contributions to scattering efficiency for nanoparticles at η_c = 0.99 (the red horizontal dashed line). This further confirms that the electric dipole and quadrupole modes are nearly degenerate at Re(ε_2) ≈ 0 and Re(ε_2) ≈ 0.6 [Re(ε_4) ≈ 0] in the thin-shell case, which agrees well with the analytical solutions of Eq. (6). For the lossy particle, however, the quadrupolar scattering contribution (red solid lines) is noticeably attenuated despite the relatively low loss of AZO, so that the total scattering (blue solid line) cannot exceed the single-channel limit (cyan solid line). As Figs. 1(c)–(e) show, decreasing η_c, that is, increasing the shell thickness, enhances both the dipole and the quadrupole resonances. Superscattering can therefore be achieved at larger shell thicknesses through enhanced and nearly degenerate dipole and quadrupole ENZMs.

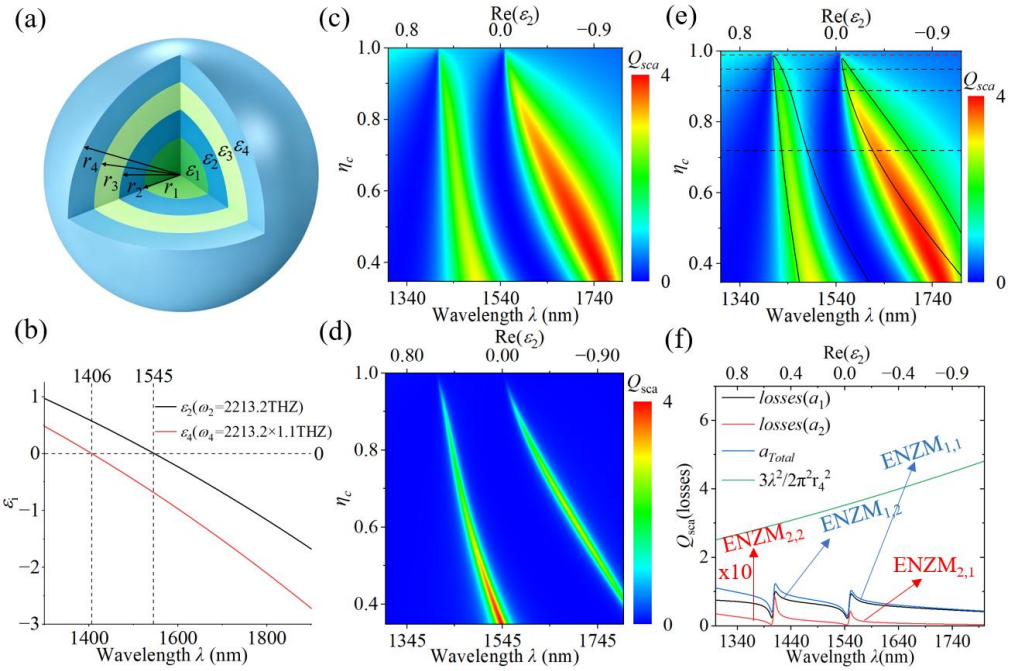


Fig. 1. (a) Schematic of the concentric multilayer core–shell nanostructure: the core radius (thickness of the first layer) is r_1, the outer radii of the three coated shells are r_2, r_3 and r_4, and the corresponding dielectric constants of the layers are ε_1, ε_2, ε_3 and ε_4. (b) Real parts of the dielectric constants ε_2 and ε_4 of AZO as functions of the incident wavelength for two different plasma frequencies in the Drude model (ω_p = 2213.2 THz for ε_2 and ω_{p1} = 1.1ω_p for ε_4). (c), (d) Scattering efficiency contributed by the electric dipole a_1 (c) and by the electric quadrupole a_2 (d) as functions of wavelength and of the core-to-outer radius ratio η_c; the top axes give Re(ε_2). (e) Map of (c) with black contours marking $Q_{sca}(a_2) > 0.1$. (f) Dipole and quadrupole contributions to the scattering efficiency for lossy nanoparticles at η_c = 0.99, as indicated by the red horizontal dashed lines in (e).

Figures 2(a)–(c) show the single-channel limit ($3\lambda^2/2\pi^2 r_4^2$), the electric dipole and quadrupole contributions, and the total scattering efficiency as functions of wavelength for lossy nanoparticles with different core-to-outer radius ratio of $\eta_c = 0.95$ [Fig. 2(a)], $\eta_c = 0.89$ [Fig. 2(b)], and $\eta_c = 0.72$ [Fig. 2(c)], as indicated by the black horizontal dashed lines in Fig. 1(e). When the shells are thin [Fig. 2(a)], the electric dipole (black line) and quadrupole (red line) resonances overlap very well, but their intensities are relatively weak, especially that of the quadrupole resonance; consequently, the total scattering (blue line) does not exceed the single-channel limit (yellow line). As η_c decreases to 0.89 and 0.72 (the shell thickness increases) [Figs. 2(b) and 2(c)], both resonances are significantly enhanced, and the total scattering efficiency (blue lines) exceeds the single-channel limit (yellow lines). However, the quadrupole resonance undergoes a more significant redshift than the dipole mode, leading to clear spectral separation of the two modes at $\eta_c = 0.72$.

Figures 2(d)–(i) show the normalized electric-field-intensity distributions at the resonant wavelengths of Figs. 2(a)–(c). For the shorter-wavelength (higher-frequency) near-degenerate ENZMs ($ENZM_{1,2}$ and $ENZM_{2,2}$), the field is mainly confined to the outermost plasmonic layer [Figs. 2(d)–(f)], whereas for the longer-wavelength (lower-frequency) near-degenerate ENZMs ($ENZM_{1,1}$ and $ENZM_{2,1}$), it is mainly confined to the innermost plasmonic layer [Figs. 2(g)–(i)]. This indicates the excitation of bulk plasmons inside the plasmonic layers, in clear contrast to conventional plasmonic modes, for which the electric field is confined to the exterior of the nanoparticle. Moreover, because the field is localized at the dielectric/AZO interfaces, the degree of degeneracy of the electric dipole and quadrupole resonances can be adjusted by varying the thickness of each shell and the permittivity of each dielectric layer.

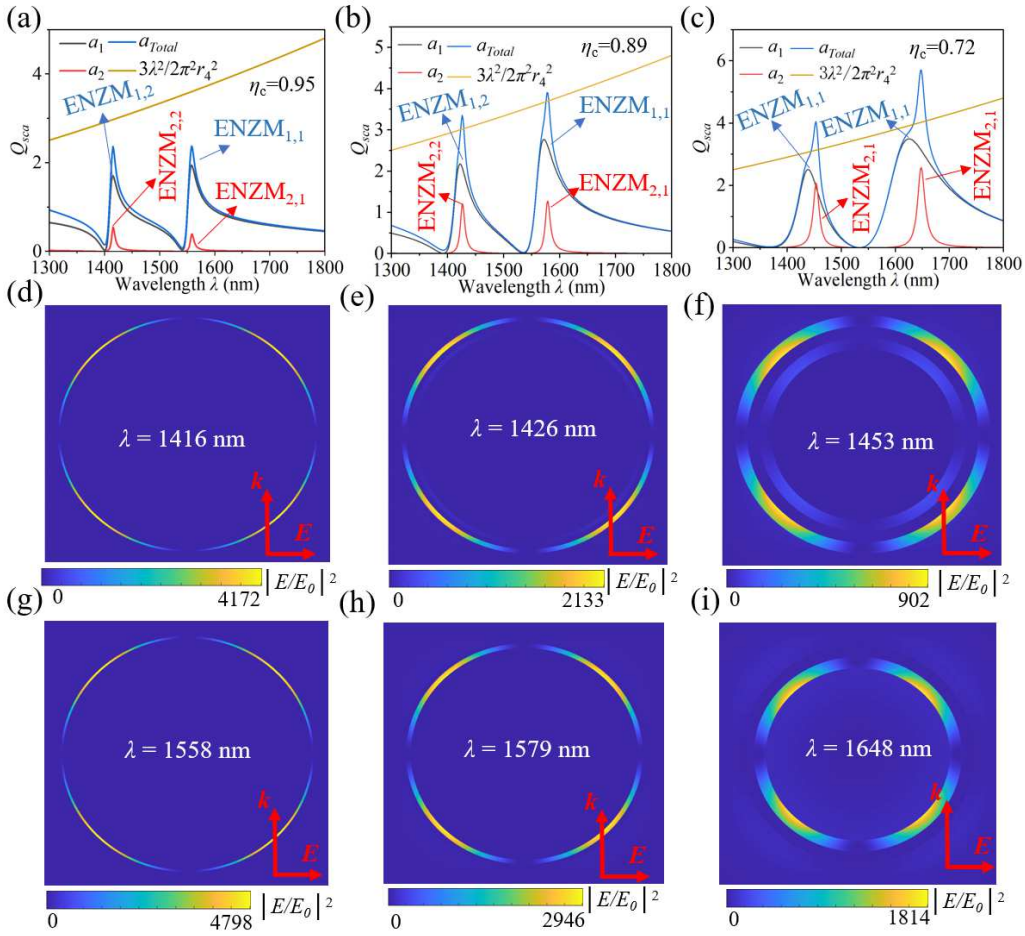


Fig. 2. (a)–(c) Single-channel limit ($3\lambda^2/2\pi^2R^2$), electric dipole (a_1) and electric quadrupole (a_2) contributions, and total scattering efficiency spectra for nanoparticles with different core-to-outer radius ratio of $\eta_c = 0.95$ (a), $\eta_c = 0.89$ (b), and $\eta_c = 0.72$ (c). (d)–(i) Electric-field-intensity enhancement distributions at the resonant wavelengths of (a)–(c) for near-degenerate ENZM$_{1,2}$ and ENZM$_{2,2}$ at shorter wavelengths ((d)–(f)) and near-degenerate ENZM$_{1,1}$ and ENZM$_{2,1}$ at longer wavelengths ((g)–(i)).

3.2. Tuning of the mode degeneracy by permittivities of the dielectric layers

Figure 3(a) shows the electric dipole (top) and quadrupole (bottom) contributions to the scattering spectra for nanoparticles with different permittivities of the dielectric core (first layer) ε_1. The core radius is fixed at $r_1 = 230$ nm, the thicknesses of the coated shells are $r_2 - r_1 = r_3 - r_2 = r_4 - r_3 = 30$ nm, and the permittivity of the third layer is fixed at $\varepsilon_3 = 3.6$. As ε_1 increases from 3 to 5, the shorter-wavelength (higher-frequency) scattering peaks of both the ENZM$_{1,2}$ and ENZM$_{2,2}$, which are associated with the bulk plasmons excited in the outermost plasmonic layer [top panels of Figs. 2(d)–(f)], remain almost unchanged. In contrast, the longer-wavelength (lower-frequency) ENZ resonance peaks

of both $ENZM_{1,1}$ and $ENZM_{2,1}$, which are associated with the bulk plasmons excited in the innermost plasmonic layer [bottom panels of Figs. 2(d)–(f)], exhibit a distinct redshift, with the dipole mode redshifts more strongly. As shown in Fig. 3(a), the longer-wavelength electric dipole and quadrupole ENZMs ($ENZM_{1,1}$ and $ENZM_{2,1}$) overlap very well when $\varepsilon_1 = 4.3$. Figure 3(b) shows the corresponding spectra for nanoparticles with different permittivities of the outermost dielectric shell (third layer) ε_3, with $\varepsilon_1 = 2.5$ and all other structural parameters identical to those of Fig. 3(a). As ε_3 increases from 3 to 5, the shorter-wavelength scattering peaks of both the electric dipole and quadrupole ENZMs ($ENZM_{1,2}$ and $ENZM_{2,2}$), exhibits only a slight redshift, while the longer-wavelength dipole and quadrupole ENZMs ($ENZM_{1,1}$ and $ENZM_{2,1}$) remain almost unchanged. The core permittivity ε_1 is therefore an efficient parameter with which the longer-wavelength electric dipole and quadrupole ENZMs can be tuned into overlap, whereas tuning the permittivity of either dielectric layer cannot further improve the overlap of the short-wavelength ENZ electric resonances.

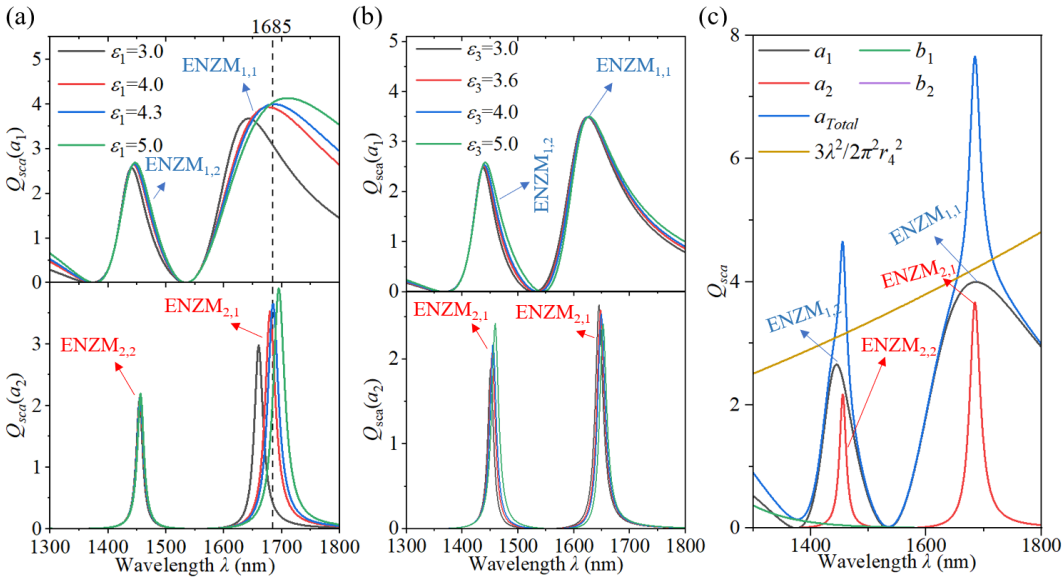


Fig. 3. (a) Electric dipole (top) and quadrupole (bottom) contributions to the scattering spectra for nanoparticles with different permittivities of the dielectric core (first layer) ε1. The core radius is fixed at r1 = 230 nm, the shell thicknesses are r2 − r1 = r3 − r2 = r4 − r3 = 30 nm, and the permittivity of the third layer is ε3 = 3.6. (b) Same as (a) for different permittivities of the outermost dielectric shell (third layer) ε3, with ε1 = 2.5 and all other parameters identical to (a). (c) Single-channel limit (3λ2/2π2r42), electric dipole and electric quadrupole contributions, and total

scattering efficiency for the optimized nanoparticle with ε1 = 4.3, ε3 = 3.6, r1 = 230 nm and r2 − r1 = r3 − r2 = r4 − r3 = 30 nm.

3.3. Tuning of the mode degeneracy by the layer thicknesses

We further illustrate how the modes are tuned by the layer thicknesses. Figures 4(a)–(c) show the electric dipole (top) and quadrupole (bottom) contributions to the scattering spectra for nanoparticles with different thicknesses of the third/fourth [Fig. 4(a)], second/third [Fig. 4(b)] and first/second [Fig. 4(c)] layer pairs. The outer radius is fixed at r_4 = 320 nm and the permittivities of the first (core) and third dielectric layers are fixed at ε_1 = 4.3 and ε_3 = 3.6, respectively. In Fig. 4(a), the thicknesses of the first and second layers are fixed at r_1 = 230 nm and $r_2 - r_1$ = 30 nm. As the thickness of the third layer increases from $r_4 - r_3$ = 5 nm to 35 nm, the thickness of the second layer decreasing correspondingly from $r_3 - r_2$ = 55 nm to 25 nm, the shorter-wavelength (higher-frequency) scattering peaks of both the electric dipole and quadrupole ENZMs ($ENZM_{1,2}$ and $ENZM_{2,2}$) redshift distinctly, the dipole mode ($ENZM_{1,2}$) more strongly. In the long-wavelength region, the electric quadrupole ENZM ($ENZM_{2,1}$) near 1685 nm remains essentially unchanged, whereas the electric ENZM ($ENZM_{1,1}$) redshifts slightly as $r_4 - r_3$ increases. When the fourth layer is relatively thin ($r_4 - r_3$ = 5 nm, black lines) the short-wavelength electric dipole and quadrupole ENZMs ($ENZM_{1,2}$ and $ENZM_{2,2}$) are well degenerate, whereas the two long-wavelength ENZMs ($ENZM_{1,1}$ and $ENZM_{2,1}$) do not overlap well. For a thicker fourth layer ($r_4 - r_3$ = 35 nm, green lines) the situation is reversed. Changing the thicknesses of the third and fourth layers simultaneously therefore cannot improve the overlap of the electric dipole and quadrupole ENZMs at both ENZ wavelengths at once.

Figure 4(b) shows the corresponding spectra for different thicknesses of the second/third layer pair, with the first and fourth layers fixed at r_1 = 230 nm and $r_4 - r_3$ = 30 nm. As the thickness of the third layer increases from $r_3 - r_2$ = 50 nm to 58 nm, the thickness of the second layer decreasing from $r_2 - r_1$ = 10 nm to 2 nm, the shorter-wavelength electric dipole ENZM ($ENZM_{1,2}$) redshifts more strongly than that of the quadrupole mode ($ENZM_{2,2}$), while the longer-wavelength ENZMs ($ENZM_{1,1}$ and $ENZM_{2,1}$) redshift at almost the same rate. Consequently, when the third layer has a thickness $r_3 - r_2$ = 56 nm (second layer $r_2 - r_1$ = 4 nm), the electric dipole and quadrupole ENZMs overlap very well at both ENZ wavelengths, as shown in Fig. 4(d).

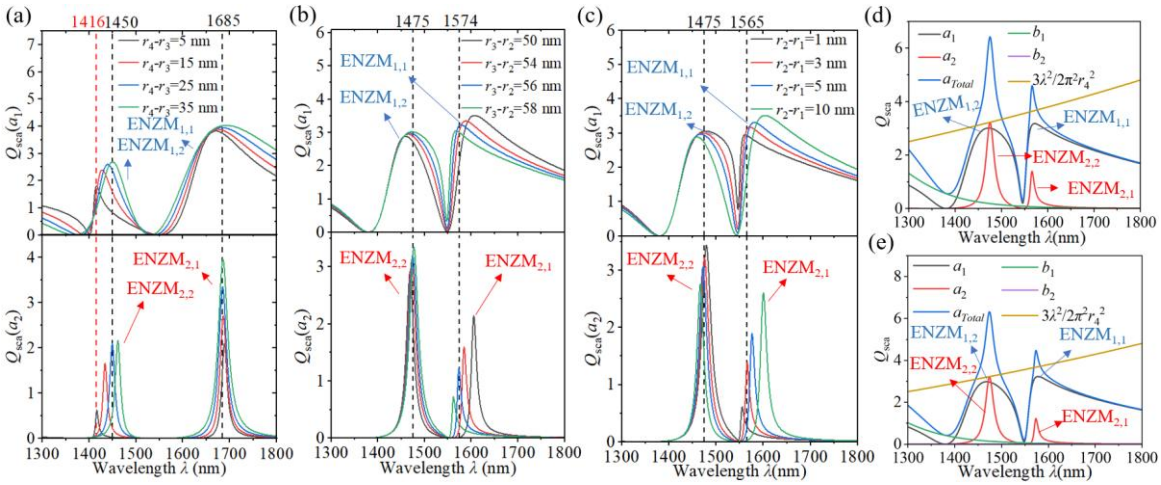


Fig. 4. (a)–(c) Electric dipole (top) and quadrupole (bottom) contributions to the scattering spectra for nanoparticles with different thicknesses of the third/fourth (a), second/third (b) and first/second (c) layers. The permittivities of the first and third dielectric layers are fixed at $\varepsilon_1 = 4.3$ and $\varepsilon_3 = 3.6$. The remaining thickness parameters are fixed at $r_1 =$ 230 nm and $r_2 - r_1 = 30$ nm in (a); $r_1 = 230$ nm and $r_4 - r_3 = 30$ nm in (b); and $r_3 - r_2 = r_4 - r_3 = 30$ nm in (c). (d), (e) Single-channel limit ($3\lambda^2/2\pi^2 r_4^2$), electric dipole and electric quadrupole contributions, and total scattering efficiency for the optimized nanoparticles: $r_1 = 257$ nm, $r_2 - r_1 = 3$ nm and $r_3 - r_2 = r_4 - r_3 = 30$ nm in (d); and $r_1 = 230$ nm, $r_3 - r_2 = 56$ nm and $r_2 - r_1 = r_4 - r_3 = 30$ nm in (e).

In Fig. 4(c) we fix $r_3 - r_2 = r_4 - r_3 = 30$ nm and vary the thickness of the second layer. As $r_2 - r_1$ increases from 1 nm to 10 nm, the core radius decreasing from 259 nm to 250 nm, the shorter-wavelength dipole ENZM ($ENZM_{1,2}$) blueshifts more strongly than that of the quadrupole ENZM ($ENZM_{2,2}$), while the longer-wavelength ENZMs ($ENZM_{1,1}$ and $ENZM_{2,1}$) redshift at almost the same rate. When the second layer is $r_2 - r_1 = 3$ nm thick, the electric dipole and quadrupole ENZMs are therefore nearly degenerate at both wavelengths, as shown in Fig. 4(e). As the second layer becomes thinner in these geometries, the longer-wavelength scattering peaks ($ENZM_{1,1}$ and $ENZM_{2,1}$) weaken significantly, especially that of the quadrupole mode ($ENZM_{2,1}$). Compared with the case of a thicker first AZO layer in Fig. 3(c), the total scattering peak near the longer wavelength decreases significantly, but it still exceeds the single-channel limit. It is worth noting that superscattering can be achieved over a wide range of thickness variations of every layer, which confirms the large tolerance of the proposed nanoparticles to size deviations introduced by fabrication (see Supplementary Section 3 for details). In addition, the interaction between the near-

degenerate electric dipole and electric quadrupole ENZMs can modulate the far-field scattering pattern, thereby enabling superdirectional scattering, as shown below.

3.4. Dual-wavelength superdirectional scattering

In this section, we demonstrate that two-wavelength super-forward and suppressed backward scattering can be realized by optimizing the layer thickness. Figures 5(a) and 5(b) present the forward [Fig. 5(a)] and backward [Fig. 5(b)] scattering efficiencies of the four-layer nanoparticles as a function of the wavelength λ and the fourth-layer thickness $r_4 - r_3$, with the thicknesses of the first (core) and fourth layers fixed at $r_1 = 230$ nm and $r_2 - r_1 = 30$ nm. The permittivities of the first (core) and third dielectric layers are fixed at $\varepsilon_1 = 4.3$ and $\varepsilon_3 = 3.6$, respectively. For clarity, the red dashed lines in Fig. 5(b) outline the regions of $Q_f > 15$ and then superimposed on the contour map of backward scattering efficiency. In addition, very low backward scattering efficiency ($Q_b < 0.5$) in Fig. 5(b) is represented by a black area to facilitate the identification of suppressed backward scattering. It is observed that when the third-layer thickness $r_4 - r_3$ lies between 0 nm and 60 nm (corresponding to the second-layer thickness $r_3 - r_2$ varying from 60 nm to 0 nm), the backward scattering efficiencies near two wavelengths of $\lambda \approx 1424$ nm and 1688 nm can be strongly suppressed [Fig. 5(b)] and mains much lower than the forward scattering efficiency Q_f [Fig. 5(a)]. The other black regions in Fig. 5(b) also correspond to the suppressed backward scattering, however, the forward scattering is also small [Fig. 5(a)]. The nanoparticle with $\varepsilon_1 = 4.3$, $\varepsilon_3 = 3.6$, $r_1 = 230$ nm, $r_2 - r_1 = 30$ nm, $r_3 - r_2 = 47$ nm, and $r_4 - r_3 = 13$ nm [the white horizontal dashed line in Fig. 5(b)] is chosen to further illustrate the superscattering with super-forward scattering at two ENZ wavelengths. Figure 5(c) shows the single-channel limit ($3\lambda^2/2\pi^2 r_4^2$), total, backward, and forward scattering efficiency spectra for such nanoparticles. It is clearly observed from Fig. 5(c) that the backward scattering efficiencies at two ENZ wavelengths $\lambda = 1424$ nm and 1688 nm are near zero (blue line), while the forward scattering efficiencies exceed 17 (red line). Figure 5(c) further demonstrates that the total scattering (black line) near two wavelengths $\lambda = 1424$ nm and 1688 nm surpasses the single-channel limit (green line). To explain the physical mechanism behind the generation of this two-wavelength super-forward and suppressed backward scattering, we present in Fig. 5d the real and imaginary parts of the Mie coefficients $3a_1$ and $5a_2$. We clearly observe from Fig. 5d that both the real and the imaginary components of $3a_1$ and $5a_2$ are equal at the two wavelengths corresponding to suppressed backward scattering ($\lambda = 1424$ nm and 1688 nm). This behavior follows directly from Eqs. (3) and (4): once the two electric channels are degenerated and oscillate in phase ($5a_2 = 3a_1$), the backward scattering can be suppressed, and the forward scattering can be enhanced. The two-dimensional angular distributions

of the normalized far-field scattered intensity are further calculated at λ = 1424 nm [Fig. 5(e)] and λ = 1688 nm [Fig. 5(f)] for incident light polarized perpendicular (*s*-polarized, black curve) and parallel (*p*-polarized, red curve). This further confirms that near-zero-backward and super-forward scattering can be achieved at both ENZ wavelengths.

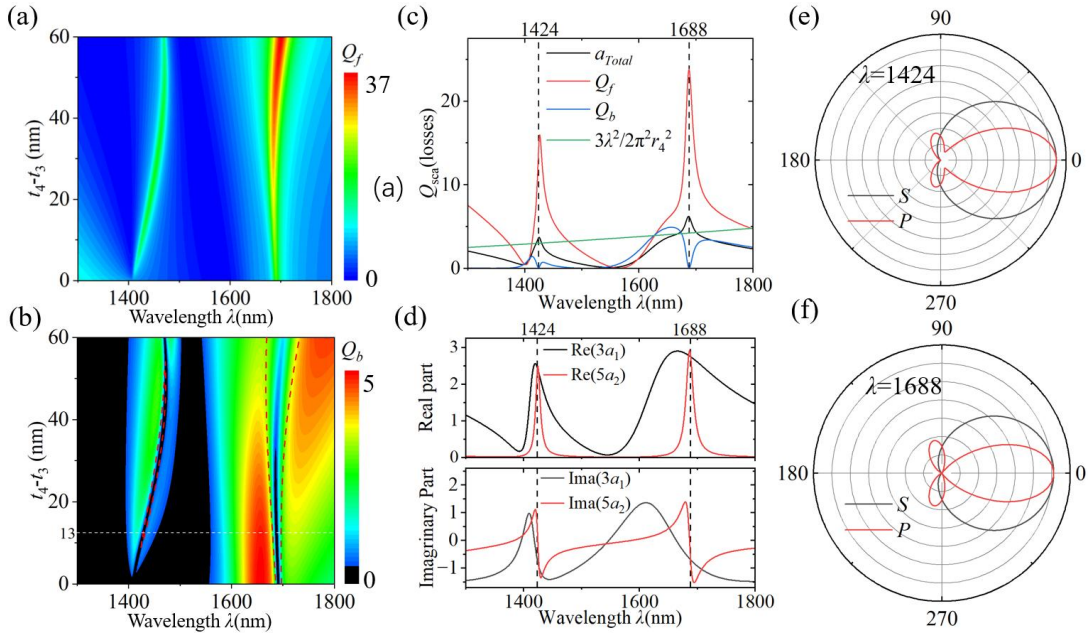


Fig. 5. (a) and (b) Forward (a) and backward (b) scattering efficiencies for four-layered nanospheres as a function of the wavelength λ and the fourth-layer thickness $r_4 - r_3$. The dark-colored region in (b) corresponds to backward scattering efficiencies below 0.5. The red dashed lines in (b) outline the regions of $Q_f > 15$. The thicknesses of the first (core) and second layers are fixed at r_1 = 230 nm and $r_2 - r_1$ = 30 nm. The permittivities of the first (core) and third dielectric layers are fixed at ε_1 = 4.3 and ε_3 = 3.6. (c) Single-channel limit ($3\lambda^2/2\pi^2r_4^2$), total, forward, and backward scattering efficiency spectra for the nanoparticle with ε_1 = 4.3, ε_3 = 3.6, r_1 = 230 nm, $r_2 - r_1$ = 20 nm, $r_3 - r_2$ = 230 nm, and $r_4 - r_3$ = 30 nm, corresponding to the white horizontal dashed line in (b). (d) Real and imaginary parts of the Mie scattering coefficients $3a_1$ and $5a_2$. (e), (f) Two-dimensional angular distributions of the normalized far-field scattered intensity at (e) λ = 1424 nm and (f) λ = 1688 nm for *s*- and *p*-polarized incident light.

4. Conclusions

We have proposed a concentric core–shell nanoparticle consisting of four alternating dielectric and aluminium-doped zinc oxide (AZO) layers with two different epsilon-near-zero (ENZ) points, and have demonstrated that it can realize superscattering and superdirectional scattering near two ENZ wavelengths. We have shown that the two AZO shells can support two electric modes with the same angular momentum (*l*) but different mode orders (*m*) near their

ENZ wavelengths and that, depending on the mode order (m) of the excited ENZ modes (ENZMs), such nanoparticles can strongly confine the electric fields within different AZO shell layers. By flexibly varying the structural parameters, both electric dipolar and quadrupolar ENZMs can be tuned to overlap at two wavelengths, where the permittivities of the two AZO shells approach zero (degenerate ENZMs), enabling two-wavelength superscattering in such a subwavelength nanoparticle. We have further demonstrated that, through the interference of degenerate electric dipolar and quadrupolar ENZMs, two-wavelength super-forward scattering can be achieved. Here, the superscattering arises mainly from the near-degenerate electric modes supported by the ENZ shells, whose ENZ wavelengths can be tuned by adjusting the aluminium doping level. Moreover, the interleaved dielectric layers provide additional structural tuning degrees of freedom that allow the two near-degenerate channels to be aligned spectrally. The Mie coefficients of the electric dipole and quadrupole modes can be readily tuned to simultaneously satisfy the condition of $3a_1 = 5a_2$ at the two ENZ wavelengths, therefore the dual super-forward and near-zero backward scattering can be realized. Owing to the unique scattering properties and design flexibility, the proposed multilayered dielectric/AZO core–shell nanoparticles hold great potential for applications in nanoantennas, biomarkers, and spectroscopy.

REFERENCES

1 Lu D, Zhu G, Li X, Xiong J, Wang D, Shi Y, Pan T, Li B, Lee LP, Xin H (2023) Dynamic monitoring of oscillatory enzyme activity of individual live bacteria via nanoplasmonic optical antennas. Nature Photonics 17:904-911. doi:10.1038/s41566-023-01265-2

2 Alaee R, Safari A, Sandoghdar V, Boyd RW (2020) Kerker effect, superscattering, and scattering dark states in atomic antennas. Phys. Rev. Research 2:043409. doi:10.1103/PhysRevResearch.2.043409

3 Cai T, Zhong Y, Liu D, Huang H, Wang D, Yang Y, Chen H, Lin X (2024) Observation of Polarization-Maintaining Near-Field Directionality. Progress In Electromagnetics Research 181:35-41. doi:10.2528/PIER24120802

4 Han J, Park SH, Jung YS, Cho YS (2024) High-performance piezoelectric energy harvesting in amorphous perovskite thin films deposited directly on a plastic substrate. Nature Communications 15:4129. doi:10.1038/s41467-024-48551-3

5 Wang J, Song Z, He M, Qian Y, Wang D, Cui Z, Feng Y, Li S, Huang B, Kong X, Han J, Wang L (2024) Light-responsive and ultrapermeable two-dimensional metal-organic framework membrane for efficient ionic energy harvesting. Nature Communications 15:2125. doi:10.1038/s41467-024-46439-w

6 Altug H, Oh SH, Maier SA, Homola J (2022) Advances and applications of nanophotonic biosensors. Nature Nanotechnology 17:5-16. doi:10.1038/s41565-021-01045-5

7 Zhang Z, Xu J, Liu K, Zhu Z (2024) Magnetic transverse unidirectional scattering and longitudinal displacement sensing in silicon nanodimer. Optics Express 32:19279-19293. doi:10.1364/OE.521725

8 Padilla WJ, Averitt RD (2022) Imaging with metamaterials. Nature Reviews Physics 4:85-100. doi:10.1038/s42254-021-00394-3

9 Li Y, Yu Q, Zhao S, Yuan Q, Zhong F, Chen X, Wang S (2025) Metasurface-Enabled Cascaded Multispectral Polarization Structures Along the Longitudinal Direction. Advanced Optical Materials 13:2403093. doi:10.1002/adom.202403093

10 Chu B, Li Y, Qin YH, Hu TZ, Zhong FC, Zeng FG, Ding P, Shao L, Du YX, Tian S, Chen Z (2023) Large-scale and tunable transparent displays based on silver nanoparticles metasurface. Nanotechnology 34:325301. doi:10.1088/1361-6528/acd388
11 Chen MJ, Yan HJ, Zhou P, Chen XY (2020) Transparent Display by the Scattering Effect of Plasmonic Au-Ag Nanoparticles. Plasmonics 15:1855-1861. doi:10.1007/s11468-020-01194-8
12 Ruan Z, Fan S (2010) Superscattering of light from subwavelength nanostructures. Physical Review Letters 105:013901. doi:10.1103/PhysRevLett.105.013901
13 Tribelsky MI, Luk'yanchuk BS (2006) Anomalous light scattering by small particles. Physical Review Letters 97:263902. doi:10.1103/PhysRevLett.97.263902
14 Qian C, Lin X, Yang Y, Xiong X, Wang H, Li E, Kaminer I, Zhang B, Chen H (2019) Experimental observation of superscattering. Physical Review Letters 122:063901. doi:10.1103/PhysRevLett.122.063901
15 Kumar R, Kajikawa K (2020) Superscattering from cylindrical hyperbolic metamaterials in the visible region. Optics Express 28:1507-1517. doi:10.1364/OE.379547
16 Liu Y, Dong H, Dong Z, Wang J (2022) Engineering multimode resonances for tunable multifrequency superscattering. Optics Express 30:1219-1227. doi:10.1364/OE.444393
17 Qian C, Lin X, Yang Y, Gao F, Shen Y, Lopez JJ, Kaminer I, Zhang B, Li E, Soljacic M (2018) Multifrequency superscattering from subwavelength hyperbolic structures. ACS Photonics 5:1506-1511. doi:10.1021/acsphotonics.7b01534
18 Zouros GP, Kolezas GD, Almpanis E, Tsakmakidis KL (2021) Three-Dimensional Giant Invisibility to Superscattering Enhancement Induced by Zeeman-Split Modes. ACS Photonics 8(5):1407-1412. doi:10.1021/acsphotonics.1c00036
19 Wang C, Chen X, Gong Z, Chen R, Hu H, Wang H, Yang Y, Low T, Zhang B, Chen H, Lin X (2024) Superscattering of light: fundamentals and applications. Rep. Prog. Phys. 87:126401. doi:10.1088/1361-6633/ad8eda
20 Kerker M, Wang DS, Giles CL (1983) Electromagnetic scattering by magnetic spheres. Journal of the Optical Society of America 73:765-767. doi:10.1364/JOSA.73.000765
21 Liu W, Miroshnichenko AE, Neshev DN, Kivshar YS (2012) Broadband unidirectional scattering by magneto-electric core–shell nanoparticles. ACS Nano 6:5489-5497. doi:10.1021/nn301398a
22 Marco MLD, Jiang T, Fang J, Lacomme S, Aymonier C (2021) Broadband forward light scattering by architectural design of core–shell silicon particles. Advanced Functional Materials 31:2100915. doi:10.1002/adfm.202100915
23 Bai Y, Zheng H, Liu J, Zhang Q, Liu S (2023) Active tuning of directional forward and backward scattering with metallic core/phase change shell nanoparticles. Optics Communications 533:129302. doi:10.1016/j.optcom.2023.129302
24 Chen Y, Chen S, Shih TM, Wang J, Yang Z (2020) Broadband unidirectional scattering in visible ranges and controllable hot-spot spatial transfer via a single nanoparticle. Applied Surface Science 528:146489. doi:10.1016/j.apsusc.2020.146489
25 Powell AW, Hibbins AP, Sambles JR (2021) Multiband superbackscattering via mode superposition in a single dielectric particle. Applied Physics Letters 118:251107. doi:10.1063/5.0054725
26 Li Y, Wan MJ, Wu WY, Chen Z, Zhan P, Wang ZL (2015) Broadband zero-backward and near-zero-forward scattering by metallo-dielectric core-shell nanoparticles. Scientific Reports 5:12491. doi:10.1038/srep12491
27 Batelbek H, Abadula R, Li P, Du P, Ren P, Gao M (2024) Efficient directional forward scattering by a single Cu@Si core-shell nanoparticle in visible regions. Optical Materials 148:114895. doi:10.1016/j.optmat.2024.114895
28 Li J, Wang H, Kivshar YS (2025) Kerker superscattering. Physical Review Applied 23:014001. doi:10.1103/PhysRevApplied.23.014001
29 Li A, Wang C, Chen X, Bian C, Zhang X, Cai W, Chen H, Lin X (2025) Kerker-superscattering via gain media. Optics Letters 50:3824-3827. doi:10.1364/OL.563151
30 Monticone F, Argyropoulos C, Alù A (2013) Multilayered plasmonic covers for comblike scattering response and optical tagging. Physical Review Letters 110:113901. doi:10.1103/PhysRevLett.110.113901
31 Schliesser A, Picqué N, Hänsch TW (2012) Mid-infrared frequency combs. Nature Photonics 6:440-449. doi:10.1038/nphoton.2012.142
32 Yan W, Zhou Z, Li H, Li Y (2023) Transmission-type photonic dipole for high-efficiency epsilon-near-zero supercoupling. Nature Communications 14:6154. doi:10.1038/s41467-023-41965-5

33 Liberal I, Mahmoud AM, Li Y, Edwards B, Engheta N (2017) Photonic doping of epsilon-near-zero media. Science 355:1058-1062. doi:10.1126/science.aal2672
34 Li H, Zhou Z, He Y, Sun W, Li Y, Liberal I, Engheta N (2022) Geometry-independent antenna based on epsilon-near-zero medium. Nature Communications 13:3568. doi:10.1038/s41467-022-31013-z
35 Kim J, Dutta A, Naik GV, Giles AJ, Bezares FJ, Ellis CT, Tischler JG, Mahmoud AM, Caglayan H, Glembocki OJ (2016) Role of epsilon-near-zero substrates in the optical response of plasmonic antennas. Optica 3:339-346. doi:10.1364/OPTICA.3.000339
36 Ghindani D, Pihlava T, Caglayan H (2022) Suppressing the spectral shift of a polarization-independent nanostructure with multiple resonances. Opt. Lett. 47:5553-5556. doi:10.1364/OL.472360
37 Wang N, Ma Y, Liu Q, Tian Y, Wang Y, Gong Q, Gu Y (2023) Resonance nesting and mode degeneracy of bilayer spherical dielectric cavities within zero-index materials. Phys. Rev. A 108:033508. doi:10.1103/PhysRevA.108.033508
38 Li Y, Yang T, Zhao S, Zhong F, Liu Q, Li M, Shao L, Yu Z, Du Y (2025) Superdirectional scattering enabled by degenerate ε-near-zero electric resonances. Physical Review A 112:033525. doi:10.1103/lq78-xr44
39 Li Y, Shao L, Zhong F, Ding P, Chen Z, Luo F, Du Y, Chen L, Lei M (2019) Generation of unconventional Fano-comb resonances in multilayered core–shell nanoparticles. Nanotechnology 30:375401. doi:10.1088/1361-6528/ab2996
40 Zhong F, Yang T, Li P, Li Y, Ge X, Lian S, Shao L, Huo H, Li Y (2026) Multi-wavelength super-directional scattering induced by degenerate electric modes in multilayered epsilon-near-zero covers. Optics Communications 620:133667. doi:10.1016/j.optcom.2026.133667
41 Naik GV, Kim J, Boltasseva A (2011) Oxides and nitrides as alternative plasmonic materials in the optical range. OPTICAL MATERIALS EXPRESS 1:1090-1099. doi:10.1364/OME.1.001090
42 Brown RGW (1983) Absorption and Scattering of Light by Small Particles. Wiley, New York.
43 Alù A, Engheta N (2005) Achieving transparency with plasmonic and metamaterial coatings. Physical Review E—Statistical, Nonlinear, and Soft Matter Physics 72:016623. doi:10.1103/PhysRevE.72.016623

Statements & Declarations

Funding

Henan Provincial Science and Technology Research Project (Nos. 252102211125), the Key Scientific Research Project of Colleges and Universities in Henan Province (Grant No. 23ZX018), National College Students Innovation and Entrepreneurship Training Program (Grant Nos. 202610485066 and 202610485082), the Scientific Research Team Plan of Zhengzhou University of Aeronautics (Grant No. 24ZHTD01002).

Competing Interests

The authors declare no competing interests.

Author Contributions

Yan Li: Data curation, Methodology, Software, Writing original draft. Pengcheng Li: Data curation, Software, Writing – original draft. Yunzhe Li: Data curation, Validation. Shuaifu Zhao: Software, Validation. Zhenchang

Song: Data curation. Xiyu Zhang: Software. Chunxia Zhang: Writing – review & editing. Li Shao: Writing – review & editing. Facheng Zhong: Conceptualization, Funding acquisition, Methodology, Supervision, Writing – review & editing. All authors reviewed the manuscript.

Data Availability

Data will be made available on request.

Supplementary Files

This is a list of supplementary files associated with this preprint. Click to download.

- supportinginformation.docx